OPEN ACCESS



Keck/NIRSPEC Studies of He1 in the Atmospheres of Two Inflated Hot Gas Giants Orbiting K Dwarfs: WASP-52b and WASP-177b

James Kirk 1 , Leonardo A. Dos Santos 2,3 , Mercedes López-Morales 1 , Munazza K. Alam 1,4 , Antonija Oklopčić 5 , Morgan MacLeod 1 , Li Zeng 6 , and George Zhou 7 , and George Zhou 1 Center for Astrophysics | Harvard & Smithsonian, 60 Garden Street, Cambridge, MA 02138, USA; james.kirk@cfa.harvard.edu 2 Space Telescope Science Institute, 3700 San Martin Drive, Baltimore, MD 21218, USA 3 Observatoire astronomique de l'Université de Genève, Chemin Pegasi 51, 1290 Versoix, Switzerland 4 Carnegie Earth & Planets Laboratory, 5241 Broad Branch Road NW, Washington, DC 20015, USA 5 Anton Pannekoek Institute for Astronomy, University of Amsterdam, 1090 GE Amsterdam, Netherlands 6 Department of Earth and Planetary Sciences, Harvard University, Cambridge, MA 02138, USA 7 Centre for Astrophysics, University of Southern Queensland, West Street, Toowoomba, QLD 4350, Australia

Abstract

Received 2021 September 17; revised 2022 May 10; accepted 2022 May 20; published 2022 June 29

We present the detection of neutral helium at 10833 Å in the atmosphere of WASP-52b and tentative evidence of helium in the atmosphere of the grazing WASP-177b, using high-resolution observations acquired with the NIRSPEC instrument on the Keck II telescope. We detect excess absorption by helium in WASP-52b's atmosphere of 3.44% \pm 0.31% (11 σ), or equivalently 66 \pm 5 atmospheric scale heights. This absorption is centered on the planet's rest frame ($\Delta v = 0.00 \pm 1.19 \ \mathrm{km \ s^{-1}}$). We model the planet's escape using a 1D Parker wind model and calculate its mass-loss rate to be \sim 1.4 \times 10¹¹ g s⁻¹, or equivalently 0.5% of its mass per gigayear. For WASP-177b, we see evidence for redshifted ($\Delta v = 6.02 \pm 1.88 \ \mathrm{km \ s^{-1}}$) helium-like absorption of 1.28% \pm 0.29% (equal to 23 \pm 5 atmospheric scale heights). However, due to residual systematics in the transmission spectrum of similar amplitude, we do not interpret this as significant evidence for He absorption in the planet's atmosphere. Using a 1D Parker wind model, we set a 3 σ upper limit on WASP-177b's escape rate of 7.9 \times 10¹⁰ g s⁻¹. Our results, taken together with recent literature detections, suggest the tentative relation between XUV irradiation and He I absorption amplitude may be shallower than previously suggested. Our results highlight how metastable helium can advance our understanding of atmospheric loss and its role in shaping the exoplanet population.

Unified Astronomy Thesaurus concepts: Exoplanet atmospheres (487); Exoplanet astronomy (486)

1. Introduction

Atmospheric escape is thought to play a key role in carving the demographics of observed exoplanets, with both the lack of short-period Neptunes (the "Neptune Desert," e.g., Mazeh et al. 2016) and the bimodal radius distribution of sub-Neptunes (the "Radius Valley," Fulton et al. 2017) the likely end-results of atmospheric loss (e.g., Lopez & Fortney 2013; Owen & Wu 2013, 2017; Owen & Lai 2018; Kurokawa & Nakamoto 2014; Allan & Vidotto 2019; Hallatt & Lee 2022). However, it is important that we build the sample of exoplanets that are observed to be *actively losing* their atmospheres so that we can measure mass-loss rates and understand how these depend on planetary and stellar parameters, while also improving our understanding of the physics of, and interaction between, planetary and stellar winds.

A new avenue to observe ongoing mass loss was recently opened by the first detection of helium in an exoplanet's atmosphere (Spake et al. 2018). This triplet, which absorbs in the near-IR at 10833 Å, can be observed from the ground and thus offers significant advantages over UV observations of Ly α , which was the primary method of observing atmospheric escape prior to 2018 (e.g., Vidal-Madjar et al. 2003; Lecavelier Des Etangs et al. 2010; Ehrenreich et al. 2015; Bourrier et al. 2018).

Original content from this work may be used under the terms of the Creative Commons Attribution 4.0 licence. Any further distribution of this work must maintain attribution to the author(s) and the title of the work, journal citation and DOI.

Indeed, there have been approximately two dozen papers targeting exoplanetary helium since 2018 (e.g., Allart et al. 2018; Nortmann et al. 2018; Kirk et al. 2020; Vissapragada et al. 2020; Zhang et al. 2021). These studies have resulted in more than 10 planets with bona fide detections of helium. This sample of planets reveals that K-type stars are the most favorable for observations of helium since they have the necessary extreme-UV (EUV) to mid-UV flux ratios to maintain a populated metastable helium state in an exoplanet's atmosphere (Oklopčić 2019). Additionally, previous studies have reported tentative evidence that planets that receive more X-ray plus EUV (XUV) irradiation show larger-amplitude helium absorption (e.g., Nortmann et al. 2018; Alonso-Floriano et al. 2019; dos Santos et al. 2020).

In this paper, we present He I observations of two inflated hot gas giant exoplanets orbiting K-type stars: WASP-52b (Hébrard et al. 2013) and WASP-177b (Turner et al. 2019).

1.1. WASP-52b

WASP-52b, discovered by Hébrard et al. (2013), is an inflated hot Saturn ($R_{\rm P}=1.253\pm0.027~R_{\rm Jup}, M_{\rm P}=0.434\pm0.024~M_{\rm Jup}, T_{\rm eq}=1315\pm26~{\rm K},$ Mancini et al. 2017) orbiting a young and active K2 dwarf (age = $0.4^{+0.3}_{-0.2}$ Gyr, $\log R'_{\rm HK}=-4.4\pm0.2$; Hébrard et al. 2013).

Previous studies of the planet's atmosphere in transmission are broadly consistent with muted spectral features, likely due to clouds in the planet's atmosphere (Kirk et al. 2016; Chen et al. 2017; Louden et al. 2017; Mancini et al. 2017; Alam et al. 2018; May et al. 2018); however, water has been detected in

the near-IR (Bruno et al. 2018, 2020), and Na, K, and H α have been detected at high resolution (Chen et al. 2017, 2020). Additionally, these previous studies have revealed in-transit light-curve anomalies from the optical to the near-IR associated with the planet occulting stellar magnetic regions (Kirk et al. 2016; Louden et al. 2017; Mancini et al. 2017; Bruno et al. 2018; May et al. 2018), highlighting the active nature of the host. Furthermore, WASP-52b is a James Webb Space Telescope (JWST) Guaranteed Time Observation target for transit and eclipse observations (PIDs: 1201 and 1224).

In Kirk et al. (2020), we identified WASP-52b as a promising target for studies of atmospheric escape via helium due to its low surface gravity, large atmospheric scale height, and K-type host. Recently, Vissapragada et al. (2020) presented a photometric transit observation of WASP-52b in a narrow filter (FWHM = 0.635 nm) centered on the He I triplet. In this filter, they measured the planet's transit depth to be $2.97\% \pm 0.13\%$, which was 1.6σ deeper than the transit depth observed by Alam et al. (2018) between 898.5 and 1030.0 nm.

In this study, we present the first high-resolution observation and detection of He I in WASP-52b's atmosphere, which extends over 66 ± 5 atmospheric scale heights (*H*).

1.2. WASP-177b

WASP-177b, discovered by Turner et al. (2019), is another inflated hot gas giant ($R_{\rm P}=1.58^{+0.66}_{-0.36}\,R_{\rm Jup},\,M_{\rm P}=0.508\pm0.038\,M_{\rm Jup},\,T_{\rm eq}=1142\pm32\,$ K) orbiting an old K2 dwarf (age = 9.7 ± 3.9 Gyr). WASP-177b is in a grazing transit configuration with an impact parameter of $0.980^{+0.092}_{-0.060}$ (Turner et al. 2019). The WASP data reveal the stellar photometry to modulate with a period of 14.86 ± 0.14 days and amplitude of 5 ± 1 mmag, indicating stellar magnetic regions. There have been no further studies of this planet.

Similar to WASP-52b, we also identified WASP-177b as a promising target for helium studies in Kirk et al. (2020) due to the planet's low surface gravity and large scale height, and the K-type host star.

In this study, we present the first atmospheric follow-up of WASP-177b. We see tentative hints of He I absorption extending across $23 \pm 5 H$; however, as we discuss in Section 4.3, we do not interpret this as significant evidence for He I absorption.

The rest of the paper is structured as follows. In Sections 2 and 3 we describe our observations and data reduction. In Section 4 we detail our data analysis and results, including our helium transmission spectra in Section 4.3. In Section 5 we present our 1D atmospheric escape modeling of WASP-52b and WASP-177b's He I transmission spectra. We discuss our results in Section 6 and conclude in Section 7.

2. Observations

We observed one transit of WASP-52b on 2020 August 1 and one transit of WASP-177b on 2020 October 4 with the NIRSPEC instrument on Keck II, as part of program N110 (PI: Kirk). This is the same instrument used in Kirk et al. (2020) for our 30σ detection of He I in the atmosphere of WASP-107b, and which has also been used by Kasper et al. (2020), Zhang et al. (2021, 2022a, 2022b), and Spake et al. (2021) for He I searches.

We used the NIRSPEC-1 filter which covers the wavelength range of 0.947–1.121 μ m (Y-band) at a nominal spectral

resolution of 25,000. For our observations of WASP-52b, we opted not to use the "Thin" blocking filter which can introduce fringing in NIRSPEC (e.g., Kasper et al. 2020). However, for our observations of WASP-177b, we incorrectly used the Thin blocking filter which did indeed lead to fringing in WASP-177's spectra, which we corrected for in our data reduction (Section 3).

Before and after each transit, we obtained 11 darks (which include the bias), 11 lamp flats, and two arcs (each comprised of 10 co-added frames with Ne, Ar, Xe, and Kr arc lamps). For our observations of WASP-52b, we took an additional two arc spectra midway through our observations to check the stability of the wavelength solution. Having found these arc spectra to be consistent with those at the start and end of our observations, we did not repeat this step for WASP-177b. We therefore acquired a total of 22 darks and 22 flats for each night, with six arcs for WASP-52b and four for WASP-177b.

For WASP-52b (J=10.6), we obtained 26 spectra with an exposure time of $1000 \, \mathrm{s}$ for the first six spectra, where clouds were overhead, and $600 \, \mathrm{s}$ for the remaining spectra. We acquired these spectra over the course of 313 minutes, and used an ABBA nod pattern to remove the sky background from our reduced spectra.

For WASP-177b (J = 10.7), we obtained 56 spectra with an exposure time of 300 s. We were able to use a shorter exposure time on this night due to better observing conditions. We acquired these spectra over the course of 310 minutes, and again used an ABBA nod pattern.

3. Data Reduction

3.1. Extracting the Wavelength-calibrated Spectra

To reduce our NIRSPEC data we used the NIRSPEC-specific REDSPEC software (McLean et al. 2003, 2007), which is written in IDL. This was the same software as we used in Kirk et al. 2020 to reduce our WASP-107b data.

In short, REDSPEC performs dark and bias subtraction, flatfielding, bad pixel interpolation, and standard spectral extraction following the spatial rectification of tilted spectra on the detector.

For the dark and flat-field corrections we median-combined the 22 darks and 22 flats to create a master dark and master flat for each night. We restricted our analysis to spectral orders 70 (1.080–1.101 μ m) and 71 (1.065–1.086 μ m) since these are the orders that cover the helium triplet at 1.0833 μ m (wavelength in vacuum). For WASP-52b, we achieved an average signal-to-noise ratio of 128 per pixel per exposure for order 70, and 134 for order 71. For WASP-177b these values were 94 and 97, respectively. For both nights, and for both orders, we used a fourth-order polynomial to correct for the tilted nature of the spectra on the detector.

The next step in REDSPEC is to perform the wavelength calibration, which we did using our arc lamp spectra. For WASP-52b, we found that a cubic polynomial was able to map the measured locations of the arc lines to the theoretical values to within 0.01 pixels.

For WASP-177b, we were unable to get a satisfactory wavelength solution from the arc lamps. This was because we chose to keep the slit position angle fixed at 12° to avoid a nearby star falling within the slit. This had the effect of shifting the stellar spectra and arc lamps, making accurate wavelength calibration difficult from the arcs. For WASP-52b, we allowed the sky to rotate on the slit, which gives the most precise radial

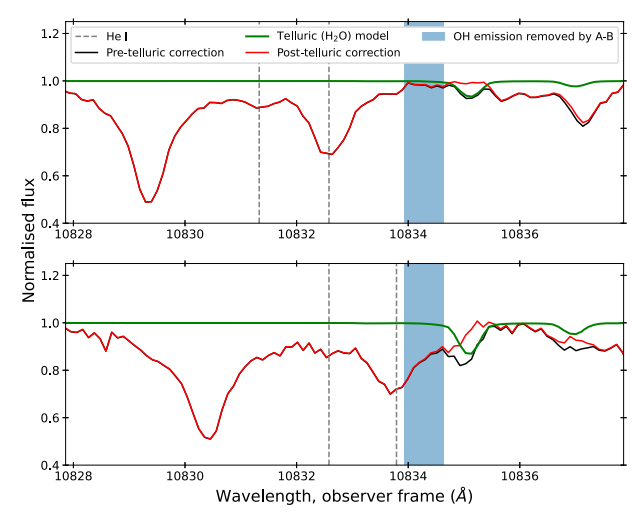


Figure 1. Example stellar spectrum of WASP-52 (top panel) and WASP-177 (bottom panel) before and after the telluric correction using molecfit (Kausch et al. 2015; Smette et al. 2015). The black spectra are the pre-corrected data, with the post-corrected data in red. The telluric models are shown in green with the shaded blue region indicating the wavelengths of strong OH emission lines that are removed by our differenced AB nod pairs. The helium triplet is denoted by the vertical dashed gray lines.

velocities for NIRSPEC, ⁸ and found the arc solution to be satisfactory. For WASP-177b, we instead used the OH emission lines in the science spectra for our wavelength calibration.

We then extracted the spectra in differenced AB nod pairs, to remove the sky background and OH emission lines, using an aperture of 15 pixels. For WASP-177's spectra, where we did use the "Thin" blocking filter (Section 2), we additionally had to perform a fringing correction. We did this using RED-SPEC's fringing correction tool, which involved manually identifying and removing peaks in the power spectra calculated for each stellar spectrum. The flux uncertainties were calculated by considering the photon noise, read noise, dark current, and sky background.

Due to the intermittent clouds in the first six frames of WASP-52b's observations, the sky background brightness varied between the A and B nod positions. This meant that a straightforward A–B subtraction did not adequately remove the OH emission lines from these frames. We experimented by adding an extra step in our spectral extraction process, by fitting the sky background with polynomials in the cross-dispersion direction, but found that this led to greater noise in the stellar spectra due to the uncertainty in the sky polynomial fit. Ultimately we found that our sigma-clipping step (Section 3.2) was able to remove the residual OH emission from these six frames. We also note that the OH emission lines were well seperated from the He I triplet for this observation (Figure 1).

3.2. Post-processing with iSpec and molecfit

Following the extraction of the wavelength-calibrated stellar spectra using REDSPEC, we then post-processed our data to continuum normalize our spectra, correct for residual wavelength shifts, and remove telluric (primarily H₂O) absorption.

To continuum normalize our data, we used iSpec (Blanco-Cuaresma et al. 2014; Blanco-Cuaresma 2019) to fit cubic

splines to a portion of each order's wavelength range (10800–10950 Å for order 70 and 10700–10850 Å for order 71), and masked the He I triplet from our continuum calculation. We focused on these portions to improve our continuum normalization in the vicinity of the He I triplet (at 10833 Å) while leaving enough telluric absorption features to allow for accurate correction.

To remove the telluric absorption, we used molecfit (Kausch et al. 2015; Smette et al. 2015), which has been used in a number of high-resolution ground-based transmission spectroscopy studies (e.g., Allart et al. 2017, 2019; Nortmann et al. 2018; Kirk et al. 2020). molecfit uses Global Data Assimilation System⁹ profiles which contain weather information for user-specified observatory coordinates, airmasses, and times. It then models the telluric absorption lines in the observed spectra using this information.

For WASP-52, order 70, we used six telluric absorption lines, free of significant stellar absorption, to constrain the molecfit model. For WASP-177, order 70, we used four telluric absorption lines to constrain the molecfit model.

We chose to fit only for the atmospheric H_2O content, with CH_4 and O_2 fixed. We also fixed the FWHM of the Lorentzian used to fit the telluric absorption to 3.5 pixels based upon our experience in analyzing NIRSPEC data, while also to overcome the impacts of the poorly removed OH emission lines in the six frames at the beginning of WASP-52b's observations (Section 3). We did this as the residual OH emission impacted molecfit's ability to model the nearby H_2O absorption if the FWHM was allowed to vary (Figure 1). We note that Zhang et al. (2021) similarly fixed this parameter to 3.5 pixels in their molecfit modeling of NIRSPEC data.

Given that order 71's wavelength coverage included fewer telluric absorption lines, we were not able to obtain a satisfactory fit to order 71 in isolation. Instead we found that using the best-fitting parameters from order 70 (i.e., depth of the water column etc.) gave good fits when applied to order 71.

Figure 1 shows example WASP-52 and WASP-177 spectra before and after the telluric correction using molecfit. This also demonstrates the proximity of the He I triplet to OH emission lines on both nights. However, aside from the first six frames for WASP-52b, our A-B nod subtraction effectively removed these emission lines from our science spectra.

There appear to be some residual oscillations in the example spectrum of WASP-177 (Figure 1, bottom panel). One possibility behind these is residual fringing from our use of the Thin blocking filter (Section 2), despite our fringing correction. However, the amplitudes of oscillations in the master spectra of WASP-177 (Figure 3) are not significantly greater than those of WASP-52 (Figure 2), for which we did not use the Thin blocking filter and thus avoided significant fringing. Therefore, we do not believe fringing is significantly affecting our results for WASP-177b.

Following the removal of telluric absorption from our spectra, we then shifted each of our spectra from the observer frame into the stellar rest frames and checked the accuracy of our wavelength solution. To shift our spectra into the stellar frame we corrected for the barycentric velocity, via astropy's (Astropy Collaboration et al. 2013, 2018) implementation of Wright & Eastman (2014)'s method, in addition to the systemic velocity and stellar reflex velocity caused by the

⁸ https://www2.keck.hawaii.edu/inst/nirspec/obs_procedures.html

https://www.ncdc.noaa.gov/data-access/model-data/model-data soglobal-data-assimilation-system-gdas

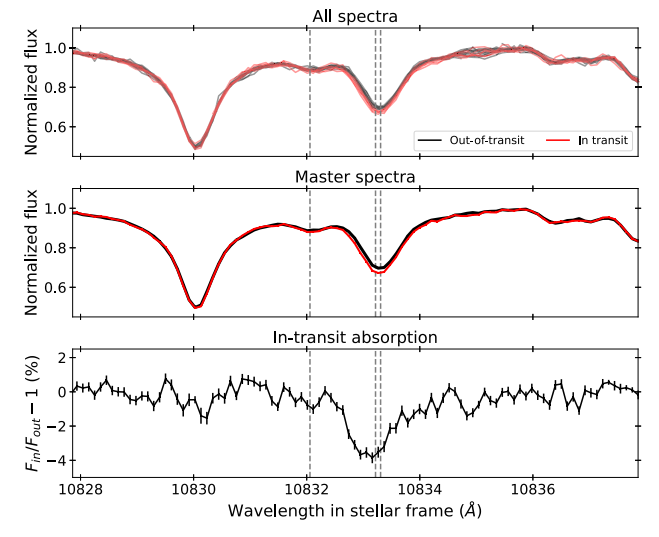


Figure 2. WASP-52's spectra centered on the helium triplet (shown by the vertical dashed lines). Top panel: individual stellar spectra, showing the out-of-transit spectra (black) and the in-transit spectra (red). Middle panel: combined "master" out-of-transit and in-transit spectra. Bottom panel: residual (excess) absorption centered on the helium triplet.

close-in gas giant (using the parameters in Table 1). To confirm our wavelength solutions, we cross-correlated our stellar spectra with Phoenix (Husser et al. 2013) model spectra for both stars. We found in both cases the wavelength solutions needed small corrections ($\sim 1~{\rm km~s^{-1}}$). Despite these being small corrections ($\sim 1/3~{\rm pixel}$) we applied them since we are sensitive to velocity shifts in the planets' He I absorption of $\sim 1~{\rm km~s^{-1}}$ (Section 4.3).

At this stage, we had normalized, telluric-corrected stellar spectra in the stellar rest frame. However, we still needed to account for the poorly removed OH emission in WASP-52b's first six frames and cosmic rays in the spectra of both WASP-52 and WASP-177. To do this, we performed a sigma-replacement method (e.g., Allart et al. 2017). Specifically, we made a median-combined spectrum for both WASP-52 and WASP-177 and compared each spectral frame to the combined median. We then replaced any data points that deviated by >4 median absolute deviations from the combined median, with the corresponding median-combined data point.

To avoid clipping out real planetary signal from our spectra, we masked the spectra within $\pm 20~\rm km~s^{-1}$ of the He I triplet in the planets' rest frames. Instead, for outliers in the He I triplet in the planets' rest frames, we removed whole frames from our analysis based on a fit to the planets' He I light curves (see Appendix A). This meant that we were neither clipping real signal nor being biased by outlying frames. By this method we removed frames 7 and 10 from order 70, and frames 8, 11, and 15 from order 71 for WASP-52 (10% of our spectra). For WASP-177 we removed no frames from order 70 and frames 47 and 56 from order 71 (2% of our spectra).

4. Data Analysis

4.1. Creating the Master Spectra

Our data analysis started with generating master in- and outof-transit spectra so that we could obtain the in-transit excess absorption signal. The in- and out-of-transit spectra were constructed by taking the weighted mean of spectra that fell between the second and third contact points, and before and after the first and fourth contact points of the transit, respectively. These contact points were determined using the ephemerides of Mancini et al. (2017) for WASP-52b and Turner et al. (2019) for WASP-177b.

Figures 2 and 3 show the individual and master spectra for both WASP-52 and WASP-177. In these figures, we have combined orders 70 and 71 into a single spectrum. Figures 2 and 3 demonstrate that there is excess absorption of ${\sim}4\%$ centered on He I for WASP-52b but no immediately apparent excess absorption for WASP-177b. We investigate this excess absorption in the following subsections.

4.2. Phase-resolved Absorption

Figures 4 and 5 show the phase-resolved excess absorption for WASP-52b and WASP-177b. These figures show each spectral frame divided by the master out-of-transit spectrum. This was performed separately for order 70 and 71 for each planet. However, we then combined the residual spectra from both orders for our analysis. For WASP-52b (Figure 4), there is clear excess in-transit absorption while there is no significant phase-resolved absorption for WASP-177b (Figure 5).

Figure 6 shows the velocity, in the stellar frame, of WASP-52b's peak excess He I absorption during its transit, calculated via fitting Gaussians to the He I transmission spectrum in each frame. This demonstrates it is consistent with both the planet's orbital velocity and no velocity shift, when considering the resolution element of NIRSPEC (12 km s⁻¹). We note that the final spectrum is at low signal-to-noise and so do not take this as evidence for blueshifted material.

4.3. Transmission Spectra

By shifting the excess absorption to each planet's rest frame (e.g., Wyttenbach et al. 2015, 2017; Allart et al. 2017), we were able to construct the He I transmission spectra for both WASP-52b and WASP-177b. These are shown in Figures 7 and 8.

Similar to our treatment of WASP-107b's transmission spectrum in Kirk et al. (2020), we initially analyzed the transmission spectra by fitting the summation of two Gaussians (which we refer to as a "double Gaussian") to quantify the excess absorption and wavelength shift. One Gaussian was centered on the weaker, bluer line at 10832.06 Å with the other centered on the two stronger, and blended, lines at 10833.22 and 10833.31 Å (vacuum wavelengths). We fitted for a wavelength shift $(\Delta \lambda)$ in the means of the two Gaussians to account for potential Doppler-shifted absorption. This wavelength shift was shared by both components of the Gaussian and was defined relative to the vacuum wavelengths of the helium triplet. The FWHM of the two Gaussians were set to be equal, given we expect the same instrumental and velocity broadening to apply to both components of the He I absorption. The amplitudes of the two Gaussians $(A_1 \text{ and } A_2)$ were allowed to vary independently. We additionally fitted for a parameter (C) to account for imperfect normalization of the transmission spectrum, which effectively moved the double Gaussian up and down in v.

In total, the transmission spectrum was fitted with five parameters (FWHM, $\Delta\lambda$, A_1 , A_2 , and C). We used Markov chain Monte Carlo (MCMC) to explore the parameter space via the emcee Python package (Foreman-Mackey et al. 2013). We ran the MCMC with 42 walkers for 10,000 steps each and discarded the first 5000 steps as burn-in. Following this initial

 Table 1

 The System Parameters of WASP-52b and WASP-177b Used in the Data Reduction and Analysis

Parameter	Symbol	Unit	WASP-52b	WASP-177b
Time of mid-transit	T_0	BJD	$2456862.79776 \pm 0.00016^{a}$	$2457994.37140 \pm 0.00028$
Orbital period	P	d	$1.74978119 \pm 0.00000052^{\mathrm{a}}$	3.071722 ± 0.000001
Orbital inclination	i	0	$85.15 \pm 0.06^{\mathrm{a}}$	$84.14^{+0.66}_{-0.83}$
Continuum transit depth	$(R_p/R_*)^2$		0.02686 ± 0.00016	$0.0185^{+0.0035}_{-0.0014}$
Semimajor axis	а	au	$0.02643 \pm 0.00055^{\mathrm{a}}$	0.03957 ± 0.00058
Scaled semimajor axis	a/R_*		7.23 ± 0.03^{a}	$9.61^{+0.42}_{-0.53}$
Stellar mass	M_*	${ m M}_{\odot}$	$0.804 \pm 0.050^{\mathrm{a}}$	0.876 ± 0.038
Planet mass	M_p	$M_{ m J}$	$0.434 \pm 0.024^{\mathrm{a}}$	0.508 ± 0.038
Planet radius	R_p	$R_{ m J}$	$1.253 \pm 0.027^{\mathrm{a}}$	$1.58^{+0.66}_{-0.36}$
Planet surface gravity	$\log g_p$	cgs	$2.84 \pm 0.02^{\mathrm{a}}$	$2.67^{+0.22}_{-0.31}$
Planet equilibrium temperature	$T_{ m eq}$	K	1315 ± 26^{a}	1142 ± 32
Semi-amplitude	K_*	$\mathrm{m}\ \mathrm{s}^{-1}$	84.3 ± 3.0^{b}	77.3 ± 5.2
Systemic velocity	γ	${\rm km~s}^{-1}$	0.48 ± 0.33^{d}	-6.41 ± 1.18^{d}
Stellar effective temperature	$T_{ m eff}$	K	5000 ± 100^{b}	5017 ± 70
Stellar metallicity	[Fe/H]	dex	0.03 ± 0.12^{b}	0.25 ± 0.04
Stellar surface gravity	$\log g$	cgs	$4.553 \pm 0.010^{\mathrm{a}}$	4.486 ± 0.049

Notes. These values are from Hébrard et al. (2013), Mancini et al. (2017), and Alam et al. (2018) for WASP-52b, and Turner et al. (2019) for WASP-177b. The systemic velocities are from Gaia DR2 (Gaia Collaboration et al. 2016, 2018).

^d Gaia DR2 (Gaia Collaboration et al. 2016, 2018).

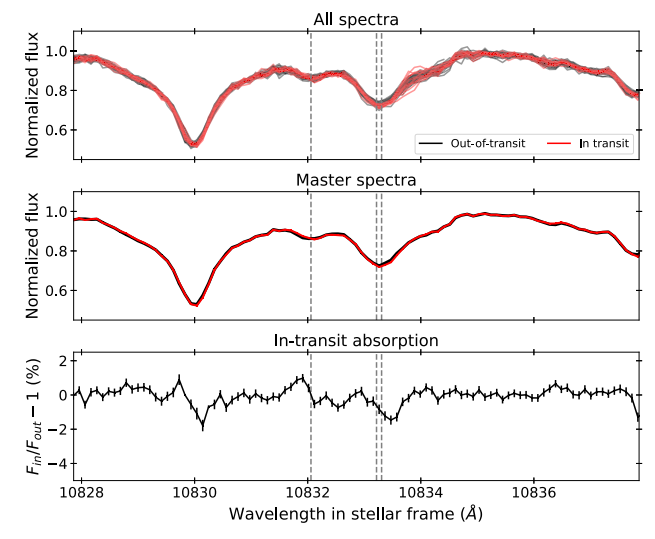


Figure 3. Same as Figure 2 but for WASP-177.

run, we then rescaled the photometric uncertainties so that the best-fitting model gave a reduced $\chi^2 = 1$ to account for red noise not taken into account by the photometric uncertainties. We then ran a second MCMC with the same setup.

For WASP-52b, we find the amplitude of the two Gaussians to be $0.26^{+0.24}_{-0.17}$ and $3.44\% \pm 0.31\%$ (11 σ), respectively. We detected no velocity offset in WASP-52b's absorption ($\Delta v = 0.00 \pm 1.19 \text{ km s}^{-1}$).

For WASP-177b, the transmission spectrum shows evidence for excess absorption around the He I triplet, although at a lower amplitude than for WASP-52b, which is also consistent with the amplitude of systematic noise in the data (Figure 8). Nevertheless, we also fitted WASP-177b's transmission spectrum with the same double Gaussian model, finding amplitudes of $0.25^{+0.23}_{-0.17}\%$ and $1.28^{+0.30}_{-0.29}\%$. However, this absorption is redshifted by $+6.02\pm1.88$ km s⁻¹.

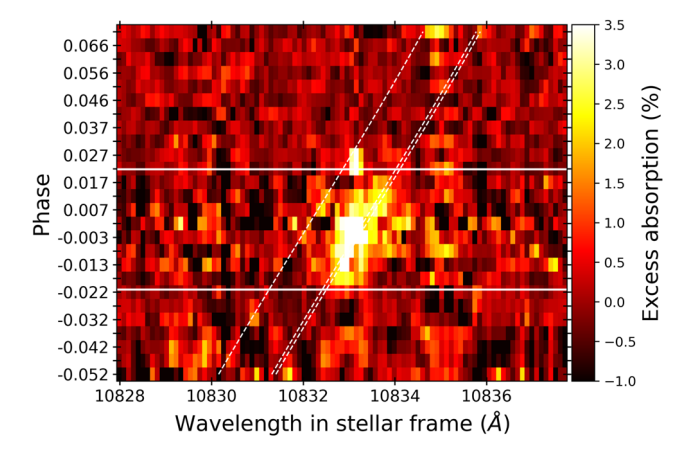


Figure 4. Phase-resolved excess absorption centered on the helium triplet during WASP-52b's transit. The wavelength is in the stellar rest frame. The horizontal white lines show the first and fourth contact points of WASP-52b's optical transit (using the ephemeris of Mancini et al. 2017). The dashed white lines indicate the planet's orbital motion.

The systematic around the Si line in WASP-177b's transmission spectrum, and this apparent redshifted He absorption, may be due to imperfect wavelength calibration for this night. This is apparent when looking at the master-in and master-out spectra of WASP-177 (Figure 3). Given the systematics in WASP-177b's transmission spectrum, we encourage additional observations to test the repeatability of this signal.

4.4. He I Light Curves

Taking the residual spectra (stellar spectra divided by the master out-of-transit spectrum) in the planet rest frame, we generated light curves by integrating the residual flux in a bin centered on the He I triplet. For the purposes of determining the transit depth as a function of bin width, we generated multiple light curves by varying the bin width from the resolution of

^a Mancini et al. (2017).

^b Hébrard et al. (2013).

^c Alam et al. (2018).

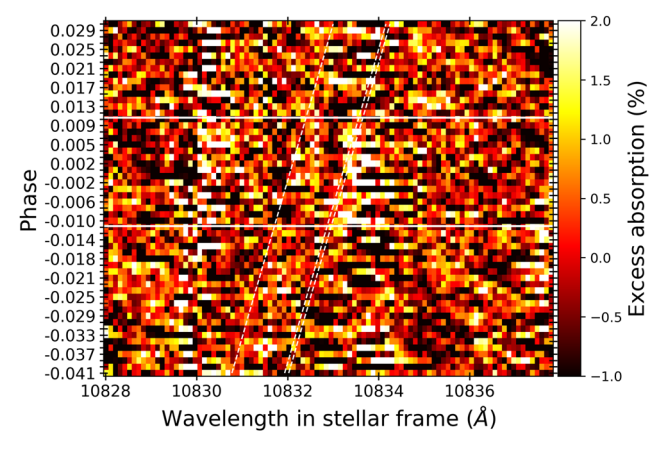


Figure 5. Phase-resolved excess absorption centered on the helium triplet during WASP-177b's transit, indicating no absorption visible by eye. See Figure 4 for details.

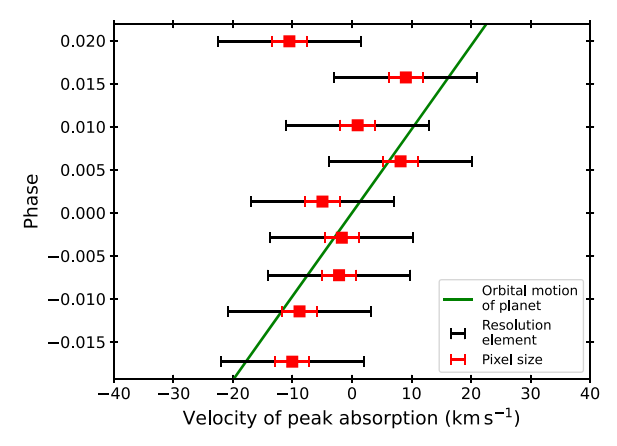


Figure 6. Velocity, in the stellar frame, of WASP-52b's peak He I absorption during transit (red squares). The red error bars show the pixel size of NIRSPEC $(0.11 \text{ Å}, 3 \text{ km s}^{-1})$ with the black error bars showing the resolution element $(12 \text{ km s}^{-1}, R = 25,000)$. The green line shows the planet's orbital motion given the parameters in Table 1. We note that the final spectrum at phase 0.020 is at low signal-to-noise and so do not take this as evidence for blueshifted material.

NIRSPEC (0.43 Å \approx 4 pixels) to 15 Å in increments of 0.5 Å. For WASP-52b, we additionally created a light curve using a bin of width 6.35 Å to match the FWHM of the filter used by Vissapragada et al. (2020).

For both WASP-52b and WASP-177b, we fixed the planets' orbital periods, time of mid-transits, scaled semimajor axes, and inclinations to the values given in Table 1. We fixed the quadratic limb-darkening coefficients to values calculated by LDTk (Parviainen & Aigrain 2015), using the stellar parameters listed in Table 1. We fitted only for R_P/R_* .

We used batman (Kreidberg 2015) to generate the light curves and fitted this using MCMC, again with emcee (Foreman-Mackey et al. 2013). In both cases we ran 20 walkers for 2000 steps each, discarding the first 1000 as burnin. We then again rescaled the photometric uncertainties to give a reduced $\chi^2=1$ and then ran the MCMC chains for a second time.

Figures 9 and 10 show the light curves corresponding to the narrowest-wavelength bins multiplied by the continuum light curves (from Alam et al. 2018 for WASP-52b and Turner et al. 2019 for WASP-177b). This multiplication is necessary to convert from *excess* absorption to *absolute* absorption. These

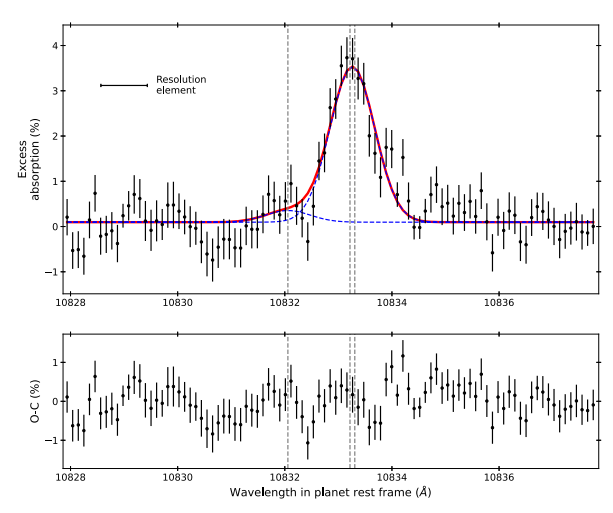


Figure 7. WASP-52b's transmission spectrum, centered on the helium triplet, whose location is shown by the vertical dashed gray lines. Top panel: transmission spectrum (in units of *excess* absorption) shown by the black data points. The red line shows the fit of the summation of two Gaussians to the transmission spectrum. The blue dashed lines show the contribution of the two components of this double Gaussian. This reveals a peak amplitude of $3.44\% \pm 0.31\%$ (11σ) and no velocity shift ($0.00 \pm 1.19 \, \mathrm{km \, s^{-1}}$). Bottom panel: residuals to the fit.

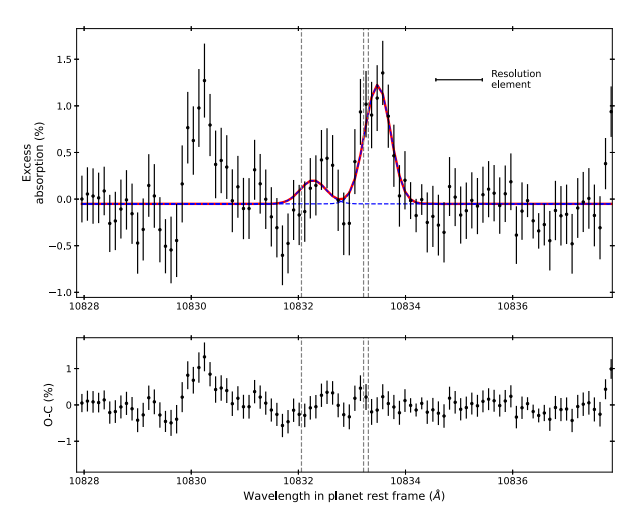
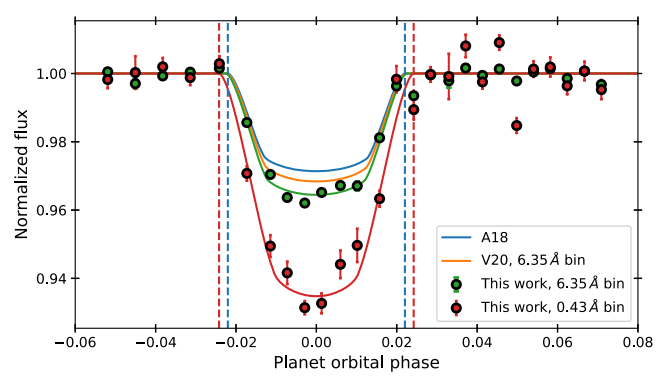


Figure 8. WASP-177b's transmission spectrum, centered on the helium triplet, which shows a peak at $1.28^{+0.39}_{-0.29}\%$ that is redshifted by $+6.02\pm1.88$ km s⁻¹. However, given the systematics in the spectrum we do not interpret this as strong evidence for helium.

figures also include the change in transit depth as a function of bin width.

Fitting WASP-52b's helium light curve, we find that the excess transit depth is $3.44\% \pm 0.36\%$ in our narrowest bin, which is consistent with our transmission spectrum (Figure 7). The light curve is largely symmetric about the midpoint. To estimate the excess transit duration we observe, we resampled our fitted transit light curve (red line, Figure 9) to a time resolution of 30 s. Comparing this with the transit duration corresponding to Alam et al. (2018)'s optical light curve, we find that WASP-52b's transit duration is 11 minutes longer at the location of the He I triplet in a 0.43 Å wide bin.

In our bin matching the filter used by Vissapragada et al. (2020; green line, Figure 9), we measure excess absorption of $0.66 \pm 0.14\%$ for WASP-52b. Vissapragada et al. place a 95th percentile upper limit on excess absorption in the helium



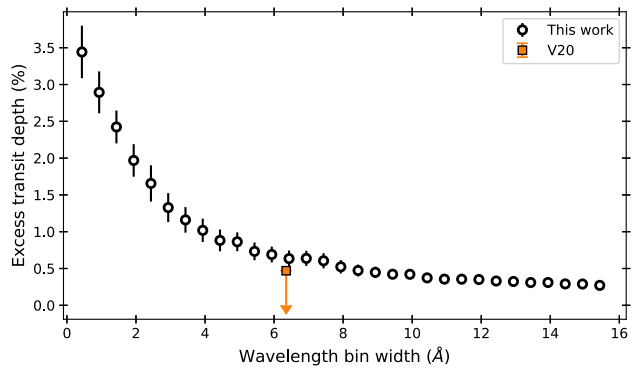


Figure 9. WASP-52b's transit light curve centered on the helium triplet. Left panel: the red points show the light curve found by integrating the residual absorption in a 0.43 Å wide bin centered on the redder two lines of the He I triplet. The red line shows a fit to these data that is then resampled to a finer time resolution. The green points show the light curve in a bin width matching the FWHM of the narrowband filter used by Vissapragada et al. (2020). The green line shows a fit to these data. The orange line shows the transit light curve observed by Vissapragada et al. (2020) and the blue line shows the "continuum" optical light curve as measured by Alam et al. (2018). The red and blue vertical dashed lines indicate the first and fourth contact points of the transit models for the helium and continuum light curves, respectively. Right panel: the excess transit depth we observe with NIRSPEC as a function of the width of the bin that we integrate over. The orange square shows the 95th percentile upper limit on WASP-52b's excess He I absorption measured by Vissapragada et al. (2020) in a 6.35 Å wide filter.

bandpass of 0.47%. Therefore in the same bandpass our result is 1.4σ deeper than that of Vissapragada et al.

The JWST will be able to observe the He I triplet with a maximum resolution of R=2700 with the G140H grism on the NIRSpec instrument, or equivalently $\Delta\lambda=4$ Å. At this resolution, we predict excess He I absorption of $\sim 1\%$ (Figure 9) for WASP-52b. This should be readily detectable if NIRSpec can reach its predicted noise floor of ~ 20 ppm (e.g., Greene et al. 2016; Batalha et al. 2017).

For WASP-177b (Figure 10), we detect no significant intransit absorption from the He I light curves.

4.5. Bootstrap Analysis

Following the approach of other ground-based high-resolution studies of narrow absorption lines (e.g., Redfield et al. 2008; Salz et al. 2018; Alonso-Floriano et al. 2019), we performed a bootstrap analysis as another check of the significance of our detection. For both orders 70 and 71, we randomly selected half of the in- and out-of-transit frames and calculated the median absorption in a 20 km s⁻¹ wide bin centered on the two redder lines of the helium triplet. We repeated this process 5000 times.

Figure 11 shows the results of this bootstrap analysis for WASP-52b, which reveals the in-minus-out distribution is >0 at 4.2σ confidence, while the out-minus-out distribution is centered on 0%, as expected.

Figure 12 shows the bootstrap analysis results for WASP-177b, revealing no significant excess in-transit absorption. We discuss this finding in the context of WASP-177b's transmission spectrum (Figure 8) in Section 6.

5. Atmospheric Escape Rate Constraints and Modeling

We interpreted the metastable He transmission spectra of WASP-52b and WASP-177b using the 1D atmospheric escape model p-winds³ (version 1.2.3; Dos Santos et al. 2022), which is based on the formulation presented in Oklopčić & Hirata (2018) and Lampón et al. (2020), and has been benchmarked against the established EVE code (e.g., Bourrier & Lecavelier des Etangs 2013; Bourrier et al. 2015). This

model treats the escaping material as an isothermal Parker wind

(Parker 1958) composed of only H+He, and finds the steady-

We fitted the co-added transmission spectra to an in-transit absorption model averaged in phase space. We used a nearby telluric absorption line to measure the shape of the spectral point-spread function (PSF) of NIRSPEC near the helium triplet. Given our modeling of the telluric absorption in the spectra (Section 3.2), we concluded the PSF is best represented by a Lorentzian with a FWHM of \sim 3.5 pixels. The implementation of p-winds takes into account both the temperature and the kinematic broadening caused by the planetary outflow.

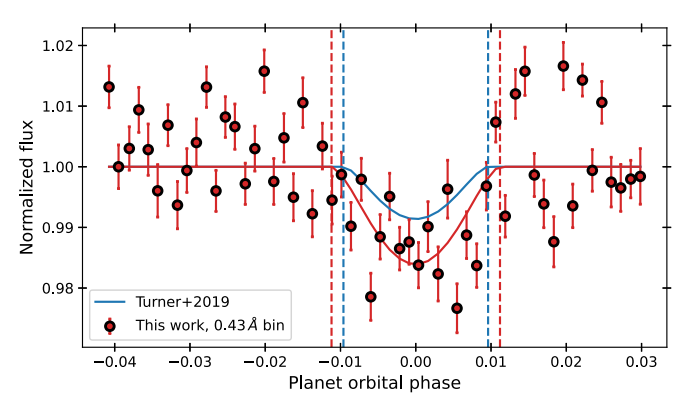
The two main free parameters of the model we fitted were the atmospheric escape rate \dot{m} and the isothermal outflow temperature T. They were explored in log-space using emcee with flat priors ($5 < \log \dot{m} < 15 \text{ g s}^{-1}$ and $3 < \log T < 5 \text{ K}$. The initial guess for the MCMC was obtained by performing a maximum likelihood estimation using the Nelder–Mead algorithm implemented in the optimize.minimize function of SciPy (Virtanen et al. 2020). Another free parameter of the fit, for which we set no prior, was the bulk radial velocity shift v_{bulk} of the absorption in relation to the planetary rest frame

We ran three different retrievals: Model (1) WASP-52b, with the H number fraction of the planetary outflow fixed to 0.90, and we explored the parameter space using 15 walkers and 7000 steps; Model (2) WASP-52b, with the H fraction set as a free parameter with a flat prior between 0.70 and 1.00, and we explored the parameter space using 20 walkers and 15,000 steps; Model (3) WASP-177b, with a fixed H fraction of 0.90, 10 walkers and 7000 steps. The lower limit of the prior on H fraction was set semi-arbitrarily to avoid numerical errors that frequently occur at low H fractions. Recent studies that simultaneously fit both Ly α and metastable He absorption in HD 189733b and GJ 3470b show that their planetary outflows have H number fractions near 0.99 (Lampón et al. 2021). But whether this is a general trend among hot gas giants remains to be tested, and will likely require more observations. Dos Santos et al. (2022) concluded that the retrieved atmospheric escape

state recombination/ionization solutions for the distribution of neutral H and He in the planetary upper atmosphere. The p-winds code also solves the radiative transfer equation to determine the in-transit absorption caused by the planet and the escaping material.

We fitted the co-added transmission spectra to an in-transit absorption model averaged in phase space. We used a pearly

¹⁰ https://github.com/ladsantos/p-winds



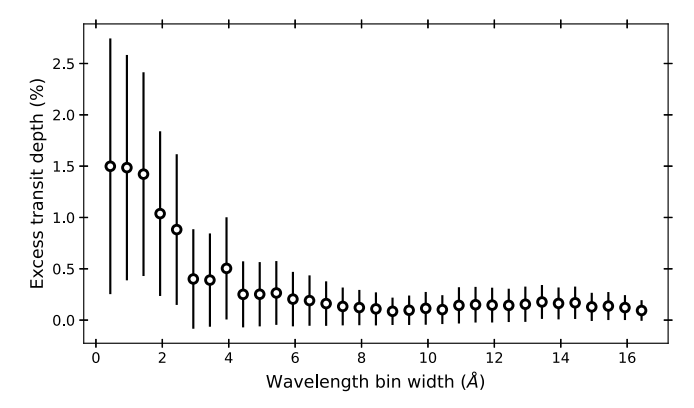


Figure 10. WASP-177b's transit light curve and the excess absorption we measure centered on the helium triplet, revealing no significant in-transit absorption. See Figure 9 for details.

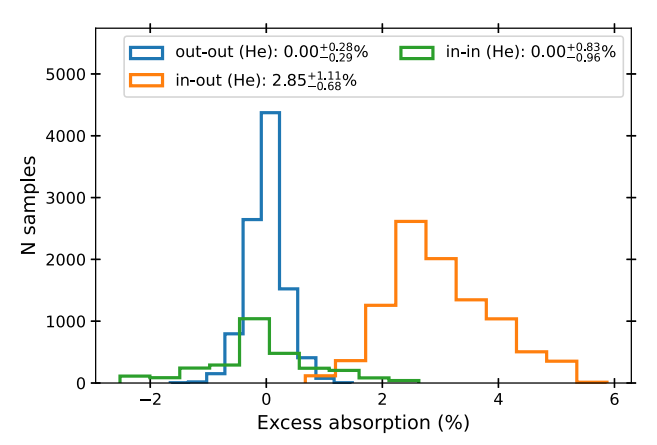


Figure 11. Our bootstrapping analysis of WASP-52b's He I absorption. The out–out (blue), in–out (orange), and in–in (green) distributions for WASP-52b in a $20~\mathrm{km~s^{-1}}$ wide bin centered on the helium triplet. For each distribution, the median, 16th, and 84th percentiles are given in the legend.

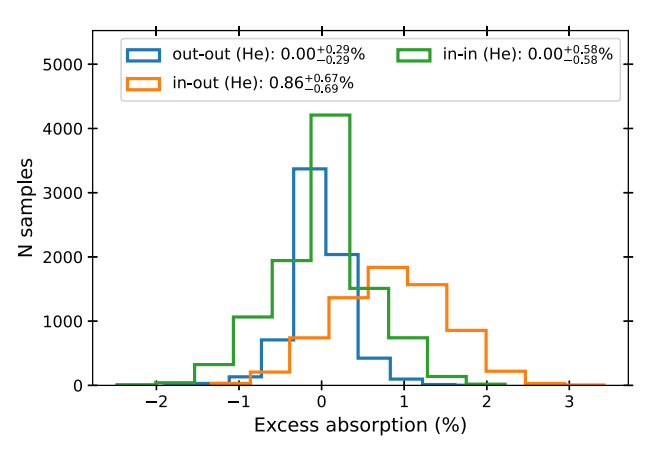


Figure 12. Distributions resulting from our bootstrap analysis for WASP-177b. See Figure 11 for details.

rate of HAT-P-11b (Allart et al. 2018) is insensitive to the H fraction for values below ~ 0.96 when using isothermal Parker wind models. For WASP-177b, we decided to not explore models where the H fraction is allowed to vary, since the detection is only tentative and we can only measure an upper limit for the atmospheric escape rate.

The relevant planetary parameters used in the fit are the same as shown in Table 1. This modeling procedure requires

knowledge about the EUV stellar spectrum (e.g., Salz et al. 2018; Palle et al. 2020). Since there is no such measurement for WASP-52 or WASP-177, we used the high-energy spectral energy distribution of eps Eri for the first and HD 40307 for the second, both measured by the MUSCLES survey (France et al. 2016). eps Eri is the same spectral type as WASP-52 (K2V), with a similar age (eps Eri: 0.4–1 Gyr, Mamajek & Hillenbrand 2008; Baines & Armstrong 2012; WASP-52: $0.4_{-0.2}^{+0.3}$ Gyr, Hébrard et al. 2013) and mass (eps Eri: $0.82 \pm 0.06 M_{\odot}$, Baines & Armstrong 2012; WASP-52: $0.804 \pm 0.050 M_{\odot}$ Mancini et al. 2017). For WASP-177, we chose to use the MUSCLES spectrum of HD 40307, since it is an older $(\sim 4.5 \text{ Gyr}) \text{ K2.5 dwarf } (0.77 \pm 0.05 M_{\odot}, \text{ e.g.}, \text{ Barnes } 2007;$ Sousa et al. 2008; Tuomi et al. 2013) slightly closer to WASP-177 in age $(9.7 \pm 3.9 \,\text{Gyr}, 0.876 \pm 0.038 \,M_{\odot}, \text{ Turner et al.})$ 2019). The stellar spectra were then scaled to the semimajor axis of WASP-52b and WASP-177b to reflect the amount of irradiation arriving at the top of the planetary atmosphere.

The results of the p-winds fit to the observed transmission spectra of WASP-52b and WASP-177b are shown in Table 2 and Figures 13, 14, and 15. The resulting model transmission spectra in comparison with the observed data are shown in Figures 16 and 17. We find that, independent of the H number fraction of the outflow, WASP-52b is most likely losing its atmosphere at a rate of 1.4×10^{11} g s⁻¹, and that the temperature of the outflow is approximately 8000 K; the bulk radial velocity of the outflow in relation to the planetary rest frame is consistent with zero. Similar to the fit results for HAT-P-11b in Dos Santos et al. (2022), allowing the H fraction to vary as a free parameter did not significantly affect the retrieved \dot{m} or T, except for increasing the uncertainties of the fit by a factor of \sim 2. In the case of WASP-177b, we find a 3σ upper limit of 7.9×10^{10} g s⁻¹ for its mass-loss rate, and an outflow temperature of approximately 6600 K.

For WASP-52b, the H number fraction is unconstrained at the 3σ level. One important insight to be gained from the posteriors and correlation maps of Figure 14 is that the retrieved escape rate is mostly insensitive to H fractions below 0.90, above which value the retrieved \dot{m} tends toward higher escape rates. There is an anti-correlation between the retrieved outflow temperature and the H fraction. These results mean that, if we are able to determine either the escape rate or outflow temperature independently of the metastable He transmission spectrum, the latter technique may be able to accurately determine the H fraction of the escaping atmosphere.

Table 21D Modeling Results for WASP-52b and WASP-177b

	$(\times 10^{11} \text{ g s}^{-1})$	<i>T</i> (K)	(km s^{-1})	H fraction
Model 1 (WASP-52b)	$1.2^{+0.5}_{-0.4}$	8100^{+1100}_{-900}	$+0.3 \pm 0.8$	Fixed at 0.90
Model 2 (WASP-52b)	$1.4^{+0.9}_{-0.5}$	7600^{+1600}_{-1200}	$+0.3\pm0.8$	>0.80 (3 σ confidence)
Model 3 (WASP-177b)	<0.79 (3 σ confidence)	6600 ± 1500	0.0 ± 0.1	Fixed at 0.90

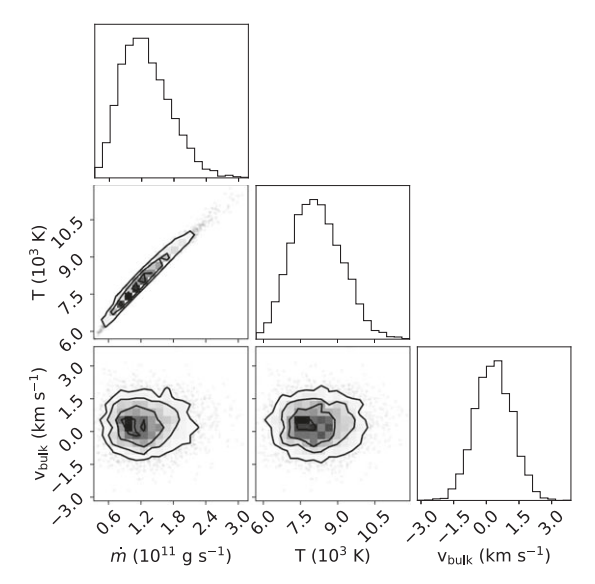


Figure 13. Posterior distributions of the atmospheric escape rate, outflow temperature, and bulk velocity of the outflow for WASP-52b. These results are based on 1D, isothermal Parker wind models fitted to the observed transmission spectrum.

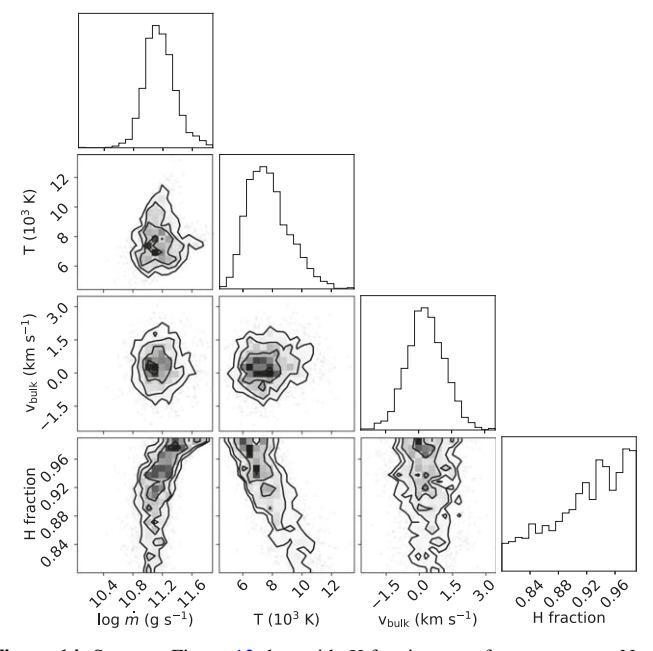


Figure 14. Same as Figure 13, but with H fraction as a free parameter. Note that the mass-loss rate is represented in logarithmic scale.

6. Discussion

6.1. He I Absorption of WASP-52b and WASP-177b

As we showed in Section 4.3, we measured significant (11σ) excess absorption by helium in WASP-52b's atmosphere and

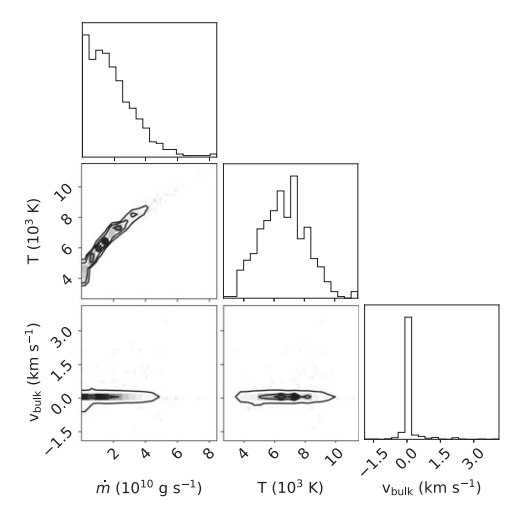


Figure 15. Same as Figure 13, but for WASP-177b

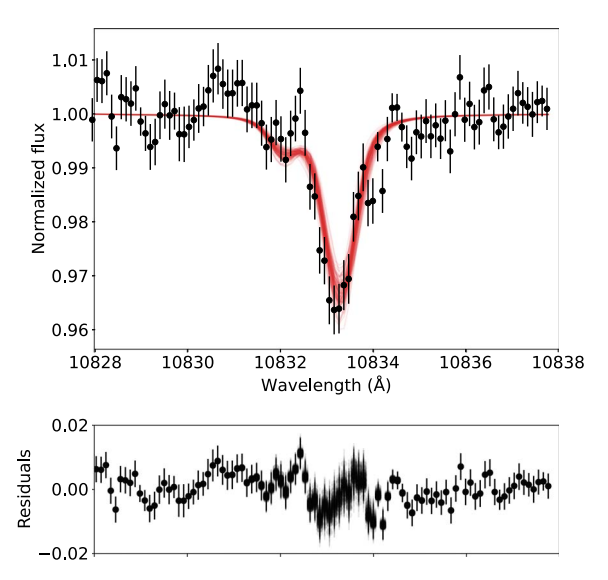


Figure 16. Sample of 100 1D, isothermal planetary wind models (red) with H fraction as a free parameter fitted to the observed transmission spectrum of WASP-52b (black symbols).

found tentative evidence for redshifted He I absorption for WASP-177b, which is not confirmed by our light curve or bootstrap analysis.

For WASP-52b, we observe excess helium absorption of $3.44\% \pm 0.31\%$. This excess absorption corresponds to 66 ± 5 atmospheric scale heights, where the scale height of the planet is 688 km using the parameters in Table 1. This in turn means that at the location of the helium triplet, and at the resolution of NIRSPEC, WASP-52b's excess helium absorption extends to $1.51 \pm 0.04~R_P$. Using the approximation of Eggleton (1983) and the planet parameters given in Table 1, we calculate

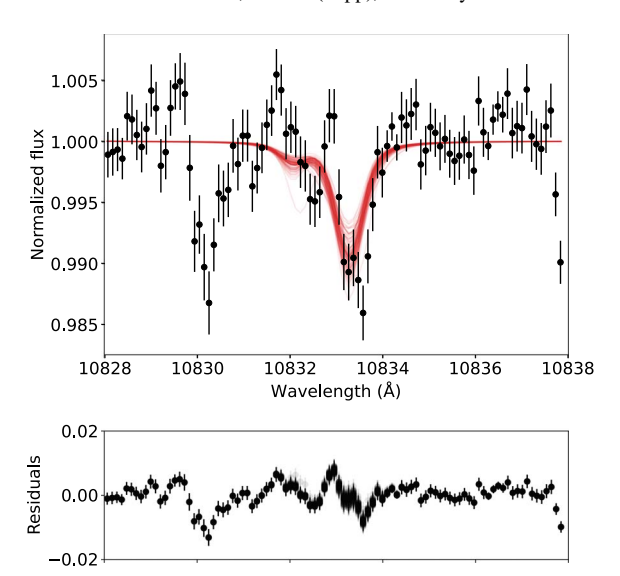


Figure 17. Same as Figure 16, but for WASP-177b and with the H fraction fixed to 0.90.

WASP-52b's Roche radius to be $1.72\,R_{\rm P}$. This means that the helium absorption we detect is close to filling the planet's Roche radius ($0.88\pm0.02\times$ the Roche radius). Using 1D isothermal Parker wind models, we calculate WASP-52b's mass-loss rate to be 1.4×10^{11} g s⁻¹ or equivalently 0.5% of its mass per Gyr. We discuss the possible consequences of 3D models in Section 6.3.

For WASP-177b, we see evidence for redshifted absorption $(\Delta v = 6.02 \pm 1.88 \text{ km s}^{-1})$ with an amplitude of $1.28^{+0.30}_{-0.29}\%$ (equal to 23 ± 5 H). However, the amplitude of this absorption is comparable to a systematic in the transmission spectrum associated with poor removal of the stellar Si line (Figure 8), which we believe may be caused by imperfect wavelength calibration for WASP-177. This redshift amounts to approximately two pixels or half the resolution element.

Furthermore, our light curve (Section 4.4) and bootstrapping (Section 4.5) do not confirm any significant He I absorption from WASP-177b. We therefore encourage additional observations of this planet to confirm or refute this possible hint of He I.

If we instead place a 3σ upper limit on WASP-177b's He I absorption based upon the standard deviation of its transmission spectrum (1.25%), we find this is equal to an upper limit of 22 H, where we calculate the scale height of the planet to be 872 km using the parameters in Table 1.

However, we also note that since the planet has a grazing transit (Figure 10), it is possible that these numbers are underestimated. Taking the R_P/R_* (0.1360 $^{+0.0129}_{-0.0052}$) and impact parameter ($b=0.980^{+0.092}_{-0.060}$) of WASP-177b (Turner et al. 2019), we calculate that at mid-transit $55^{+21}_{-14}\%$ of WASP-177b's atmosphere is being probed. Therefore, taking the 1σ lower bound on the amount of the planet's atmosphere that is being probed at mid-transit (41%), and scaling our 22 H upper limit, the upper limit on WASP-177b's He I absorption could be as high as 54 H, assuming spherically symmetric He I absorption.

6.2. Stellar Activity

WASP-52 is an active star with numerous observations of magnetic activity regions occulted during transits of the planet

(Kirk et al. 2016; Louden et al. 2017; Mancini et al. 2017; Bruno et al. 2018; May et al. 2018). Despite this activity, we interpret the helium absorption we detect as being planetary, not stellar, in nature. In a simulation study, Cauley et al. 2018 showed that the 10833 Å He I triplet could be contaminated at the 0.1% level in specific cases, but that these would likely lead to a *dilution* of the signal, not an enhancement/spurious detection. This is significantly smaller than the $3.44\% \pm 0.31\%$ signal that we observe (Figure 7). Additionally, in Chen et al.'s (2020) study of WASP-52b's H- α absorption, the authors demonstrated that the $0.86\% \pm 0.13\%$ absorption they detected was not replicated in the activity indicator lines they used as a control sample. Finally, the good agreement between our study and that of Vissapragada et al. (2020; Figure 9), for which the observation epochs were separated by a year, suggests nonvariable planetary absorption. Taken together, we attribute the absorption we detect to WASP-52b's atmosphere, not stellar activity.

For WASP-177, Turner et al. (2019) attributed modulation in its photometry to active regions on the host star. However, given it is the same spectral type as WASP-52 but older $(9.7\pm3.9~{\rm Gyr}$ as opposed to $0.4^{+0.3}_{-0.2}~{\rm Gyr}$; Hébrard et al. 2013), similar arguments apply and therefore we do not believe that our observations of WASP-177b are significantly impacted by activity.

6.3. On the Possible Consequences of 3D Models of WASP-52b's Atmospheric Escape

We have so far discussed inferences from spherical models of escaping planetary outflows. In reality, planetary winds escape in an orbiting frame and are shaped by the stellar wind environment of their host stars. Thus, the geometry of the escaped planetary material can be distorted by orbital effects and the interaction with the stellar wind (e.g., McCann et al. 2019; Wang & Dai 2021). This can, in turn, affect the overall strength of the absorption signal and how it relates to the properties of the planetary outflow, such as the mass-loss rate.

These effects can only be fully studied in three dimensions with simulation models catered to a particular planet's parameters. Performing Bayesian inference with these sorts of models remains computationally intractable because of their expense. However, our use of 1D atmospheric profiles to infer the planetary mass-loss rate is justified by the fact that the both WASP-52b's helium absorption (Figure 7) and light curve (Figure 9) are symmetric, which also suggests we are probing the thermosphere and not the exosphere (e.g., see Figure 4 of Allart et al. 2019).

Recent 3D simulations by MacLeod & Oklopčić (2022) show that, in cases of relatively weak and moderate confinement of the planetary outflow by the stellar wind, the helium absorption originates from a region of unshocked planetary material which is not significantly affected by the interaction with the stellar wind (see Figure 2 of MacLeod & Oklopčić 2022). As a result, the helium light curve has a high degree of symmetry around the transit midpoint, similar to what we see for WASP-52b (Figure 9), and the absorption depth is consistent with the predictions of the spherically symmetric Parker wind models which do not include stellar winds at all. In the case of strong confinement by the stellar wind, the planetary outflow gets distorted, which results in a boosted absorption signal (compared to the 1D Parker wind

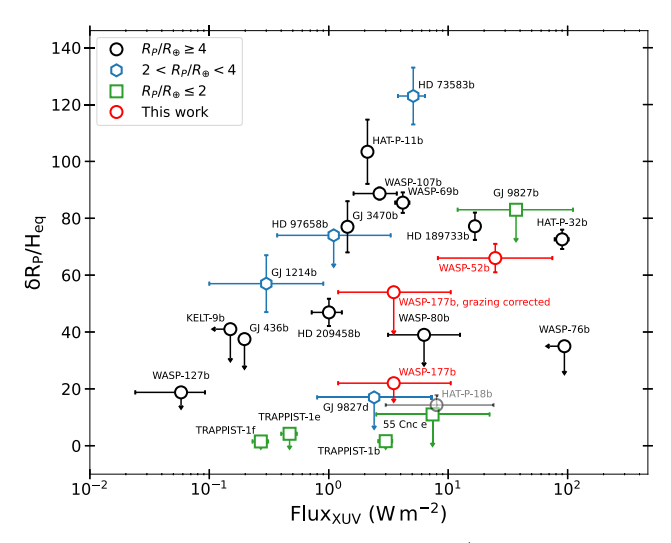


Figure 18. Published detections and non-detections/upper-limits of helium absorption in the literature, separated into gas giants (black circles), sub-Neptunes (blue hexagons) and super-Earths/Earths (green squares). These are plotted in terms of the XUV flux received against amplitude of excess helium absorption observed, in units of the planets' atmospheric scale heights. The red circles show our new results for WASP-52b and WASP-177b, including the upper limit after correcting for the planet's grazing transit configuration. We reiterate that WASP-52 and WASP-177 do not have measured XUV fluxes, but instead we use appropriate spectra from the MUSCLES survey (France et al. 2016) and assume these are accurate to within a factor of three (see the text for details). We note that HAT-P-18b is shown with a lower opacity due to its detection with photometry (Paragas et al. 2021) which could be underestimating the full amplitude of this planet's absorption. The references for these planets are given in Table 3.

model predictions) and an asymmetric light curve with a prolonged helium egress, i.e., a helium "tail."

Given the predicted $\sim 1\%$ amplitude of WASP-52b's He I absorption at the resolution of the JWST (Section 4.4), future observations with the JWST could provide a more finely sampled light curve which is needed to fully assess the impact of stellar wind on the escaping material.

6.4. On the Potential Correlation between He I Absorption and XUV Irradiation

Previous studies of exoplanetary helium absorption suggested evidence for a potential relation between XUV irradiation and the amplitude of He I absorption observed for gas giant exoplanets (e.g., Nortmann et al. 2018; Alonso-Floriano et al. 2019; dos Santos et al. 2020). However, more recent results (Casasayas-Barris et al. 2021; Fossati et al. 2022) are in disagreement with this tentative relation.

Figure 18 shows all exoplanets with well-constrained He I absorption 11, along with our new findings for WASP-52b and WASP-177b. Following our 1D modeling (Section 5), we adopted eps Eri for WASP-52 and HD 40307 for WASP-177 to calculate the planets' XUV irradiation. Following Kasper et al. (2020) and Zhang et al. (2020), we assume that our estimated XUV fluxes are accurate to within a factor of three, based on typical uncertainties in the reconstruction of stellar EUV fluxes (e.g., Oklopčić 2019). However, this is likely an underestimation, since the gyrochronological and isochronal ages for WASP-52 and WASP-177 (Hébrard et al. 2013; Mancini et al. 2017; Turner et al. 2019) lead to significantly different XUV fluxes when using empirical age—XUV luminosity relations

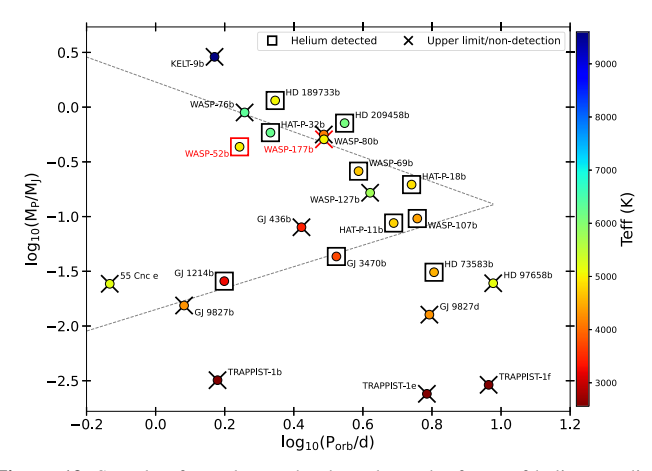


Figure 19. Sample of exoplanets that have been the focus of helium studies, along with the boundaries of the Neptune Desert as defined by Mazeh et al. (2016; dashed gray lines). Each data point's color is related to the effective temperature of its host star. Those exoplanets with detections of helium are shown within squares and those with upper limits/non-detections are shown with crosses. The sizes of the uncertainties are smaller than the plot symbols. WASP-52b and WASP-177b (this work) are shown in red. See Table 3 for references.

(e.g., Sanz-Forcada et al. 2011). For the purposes of Figure 18, we estimate $F_{XUV}=24.8^{+49.7}_{-16.6}~W~m^{-2}$ for WASP-52b and $F_{XUV}=3.5^{+7.0}_{-2.3}~W~m^{-2}$ for WASP-177b.

Our new results, taken together with recent results for WASP-76b (Casasayas-Barris et al. 2021), HAT-P-18b (Paragas et al. 2021), WASP-80b (Fossati et al. 2022), and HAT-P-32b (Czesla et al. 2022), suggest a shallower relation between XUV irradiation and He I, if indeed such a relation exists. However, it is important to consider that WASP-177b's transit is grazing, and so its amplitude may be as large as 54 H (Section 6.1), while HAT-P-18b's detection resulted from a narrowband filter which may also be underestimating the full amplitude of its He I absorption. Futhermore, the observations of WASP-76b were hampered by telluric absorption (Casasayas-Barris et al. 2021). Therefore additional observations are needed to test the existence of such a relation.

While this paper was under review, Poppenhaeger (2022) published a subset of literature He I results, finding that the amplitude of exoplanetary He I absorption is more strongly correlated to narrowband EUV fluxes that take into account the stellar coronal iron abundances. We will look for a similar correlation in the updated sample of He I-targeted exoplanets in a future work.

6.5. Helium Studies and the Neptune Desert

The Neptune Desert is the name given to the observed dearth of short-period Neptunes in the exoplanet population (e.g., Mazeh et al. 2016). It has been suggested that this is the result of atmospheric loss; planets that initially fell within this desert were quickly stripped of their atmospheres and subsequently migrated out of the desert toward smaller masses and radii (e.g., Kurokawa & Nakamoto 2014; Matsakos & Königl 2016; Owen & Lai 2018; Allan & Vidotto 2019; Hallatt & Lee 2022).

Given the rapid increase in the number of exoplanets that have been the focus of published helium observations, we can start to interpret these in the context of the Neptune Desert. Figure 19 shows the sample of published exoplanetary helium observations (Table 3) along with the boundaries of the Neptune Desert as defined by Mazeh et al. (2016). This figure

 $[\]overline{^{11}}$ All planets with detected He I absorption or upper limits <100 H.

 Table 3

 Published Detections and Robust Upper Limits of Exoplanetary Helium Absorption in the Literature as Plotted in Figures 18 and 19

			· · · · · · · · · · · · · · · · · · ·
Planet	$F_{XUV} (W m^{-2})$	$\delta R_P/H_{ m eq}$	References
WASP-69b	4.170 ± 0.566^{a}	85.5 ± 3.6	Nortmann et al. (2018), (also Vissapragada et al. 2020)
HD 189733b	16.75 ± 0.028^{a}	77.2 ± 4.8	Nortmann et al. (2018), (also Salz et al. 2018; Guilluy et al. 2020)
HD 209458b	1.004 ± 0.284^{a}	46.9 ± 4.8	Alonso-Floriano et al. (2019), (also Nortmann et al. 2018)
HAT-P-11b	2.109 ± 0.124^{a}	103.4 ± 11.3	Allart et al. (2018), (also Mansfield et al. 2018)
WASP-107b	2.664 ± 1.05^{a}	88.7 ± 2.1	Kirk et al. (2020), (also Spake et al. 2018; Allart et al. 2019; Spake et al. 2021)
GJ 436b	$0.197 \pm 0.007^{\mathrm{a}}$	€37.5	Nortmann et al. (2018)
KELT-9b	≤0.15 ^a	≤ 41	Nortmann et al. (2018)
WASP-127b	0.058 ± 0.034^{a}	≤18.77	dos Santos et al. (2020)
GJ 1214b	$0.3^{+0.6a}_{-0.2}$	57 ± 10	Orell-Miquel et al. (2022),
			(also Kasper et al. 2020; Petit dit de la Roche et al. 2020)
GJ 9827d	$2.4^{+4.8a}_{-1.6}$	≤17	Kasper et al. (2020), (also Carleo et al. 2021)
HD 97658b	$1.1^{+2.2}_{-0.73}$ a	≤ 74	Kasper et al. (2020)
GJ 3470b	1.435 ± 0.008^{a}	77 ± 9	Palle et al. (2020), (also Ninan et al. 2020)
55 Cnc e	$7.4^{+14.8b}_{-4.9}$	≤11	Zhang et al. (2020)
HAT-P-18b	8^{+16b}_{-5}	14.3 ± 3.5	Paragas et al. (2021)
HD 73583b/TOI-560b	5.1 ± 1.3^{b}	123 ± 10	Zhang et al. (2022a)
HAT-P-32b	90 ± 12^{a}	$72.6 \pm 3.4^{\circ}$	Czesla et al. (2022)
WASP-80b	$6.281^{+6.281b}_{-3.141}$	≤ 39	Fossati et al. (2021)
WASP-76b	≤94 ^a	≤35	Casasayas-Barris et al. (2021)
GJ 9827b	37^{+74b}_{-25}	≤ 83	Carleo et al. (2021)
TRAPPIST-1b	$3 \pm + 0.4^{b,d}$	≤1.6	Krishnamurthy et al. (2021)
TRAPPIST-1e	$0.4 \pm 0.07^{ m b,d}$	≤4.2	Krishnamurthy et al. (2021)
TRAPPIST-1f	$0.27 \pm +0.04^{\rm b,d}$	€1.5	Krishnamurthy et al. (2021)
WASP-52b	24.8 ^{+49.7a}	66 ± 5	This work
WASP-177b	$3.5^{+7.0a}_{-2.3}$	€22	This work

Notes. The first reference in the reference column is that from which the values are taken or derived. Additional references to studies of these planets are also given.

reiterates the finding of Oklopčić (2019) that K stars are the most favorable for studies of helium as most exoplanets with helium detections orbit stars with $T_{\rm eff} \approx 5000$ K.

If atmospheric loss is responsible for the Neptune Desert, we might expect planets falling within the boundaries of the desert to be losing their atmospheres. Figure 19 shows that several exoplanets with non-detections of helium absorption reside within the boundaries of the desert. However, since these planets do not orbit K stars, it is possible that they are losing their atmospheres but helium is not a sensitive probe.

Considering only WASP-52b and WASP-177b on Figure 19, we see that WASP-52b sits inside the Neptune Desert and is losing its atmosphere at a significant rate. WASP-177b sits at the edge of the desert and due to systematics in our data and its grazing transit, we cannot say with confidence whether the planet is or is not losing its atmosphere. Nevertheless, Figure 19 demonstrates the potential of the 10830 Å He I triplet to probe the origins of the Neptune Desert, which motivates further observations of exoplanets in this parameter space.

7. Conclusions

In this study, we used the NIRSPEC instrument on the Keck II telescope to search for helium at 10833 Å in the atmospheres of the inflated hot gas giants WASP-52b and WASP-177b, both of which orbit K-type stars.

We detect significant excess absorption by helium in the atmosphere of WASP-52b, with an amplitude of $3.44 \pm 0.31\%$ (11σ), or equivalently, 66 ± 5 atmospheric scale heights, that is centered in the planet's rest frame ($\Delta v = 0.00 \pm 1.19 \text{ km s}^{-1}$). This absorption amplitude means that the planet is close to filling its Roche lobe. Using 1D isothermal Parker wind models, we find that WASP-52b is losing its mass at a rate of $\sim 1.4 \times 10^{11} \text{ g s}^{-1}$, or equivalently, 0.5% of its mass per gigayear. This is the first high-resolution detection of WASP-52b's escaping atmosphere.

For WASP-177b, we find evidence for helium-like absorption of $1.28^{+0.30}_{-0.29}\%$ in the planet's transmission spectrum. However, its anomalous redshift ($\Delta v = +6.02 \pm 1.88 \text{ km s}^{-1}$) combined with a lack of confirmation from light-curve and bootstrap analyses means we do not interpret this as significant evidence for a detection of He I in the planet's atmosphere. We therefore place a 3σ upper limit on the planet's absorption of 1.25%, or equivalently 22 atmospheric scale heights. However, because of the planet's grazing transit we may be underestimating the true extent of its helium absorption, which could be as much as 54 scale heights. Our 1D modeling of WASP-177b's helium transmission spectrum places a 3σ upper limit on the planet's escape rate of $7.9 \times 10^{10} \text{ g s}^{-1}$.

Our results, taken together with recent results in the literature, raise doubts about the existence of a relation between XUV irradiation and He I amplitude. Nevertheless, our results highlight the important role that He I can play in understanding

^a For $\lambda < 504$ Å.

^b For λ < 912 Å.

^c Error calculated assuming same fractional uncertainty as in the equivalent width.

^d Calculated from Wheatley et al. (2017).

exoplanet atmosphere escape and how it impacts the exoplanet population through features like the Neptune Desert.

The data presented herein were obtained at the W. M. Keck Observatory, which is operated as a scientific partnership among the California Institute of Technology, the University of California and the National Aeronautics and Space Administration. The Observatory was made possible by the generous financial support of the W. M. Keck Foundation. The authors wish to recognize and acknowledge the very significant cultural role and reverence that the summit of Maunakea has always had within the indigenous Hawaiian community. We are most fortunate to have the opportunity to conduct observations from this mountain.

We are grateful to our support astronomer Greg Doppmann for his guidance during the observations and data reduction. L. A.D.S. acknowledges financial support from the European Research Council (ERC) under the European Union's Horizon 2020 research and innovation program, project FOUR ACES (grant agreement No. 724427); this work has partially been carried out in the frame of the National Centre for Competence in Research PlanetS supported by the Swiss National Science Foundation (SNSF). L.Z. would like to thank the support by the U.S. Department of Energy under awards DE-NA0003904 and DE-FOA0002633 (to S.B.J., principal investigator, and collaborator Li Zeng) with Harvard University and by the Sandia Z Fundamental Science Program. This research represents the authors views and not those of the Department of Energy. Finally, we also thank the anonymous referee for their comments which led to an improvement in the quality of the manuscript.

Facility: Keck(NIRSPEC).

Software: Astropy (Astropy Collaboration et al. 2013, 2018), Batman (Kreidberg 2015), emcee (Foreman-Mackey et al. 2013), iSpec (Blanco-Cuaresma et al. 2014; Blanco-Cuaresma 2019), LDTk (Parviainen & Aigrain 2015), Matplotlib (Hunter 2007), molecfit (Kausch et al. 2015; Smette et al. 2015), Numpy (Van Der Walt et al. 2011), p-winds (Dos Santos et al. 2022; dos Santos & Vissapragada 2021), RED-SPEC (McLean et al. 2003, 2007), Scipy (Virtanen et al. 2020).

Appendix A Sigma-clipping of Frames

As described in Section 2, we opted to exclude certain outlying frames from our analyses due to a combination of poor observing conditions and cosmic rays.

We created transit light curves with our data in 0.43 Å wide bins (equal to one resolution element) centered on the mean of the redder two lines of the He I triplet (10833.261 Å) for orders 70 and 71 separately. We then fitted an analytic transit light curve following the procedure described in Section 4.4 to the resulting light curves. We excluded those frames that lay >4 median absolute deviations away from this fitted model. Figure 20 shows this fitted model along with the frames that were rejected. By this method we rejected frames 7 and 10 from order 70, and frames 8, 11, and 15 from order 71 (10% of the total frames) for WASP-52b. For WASP-177b, we excluded no frames from order 70 and two frames from order 71 (47 and 56, 2% of our spectra), as shown in Figure 21. Figures 20 and 21 also demonstrate which frames were used to define the in-transit, out-of-transit, ingress, and egress frames.

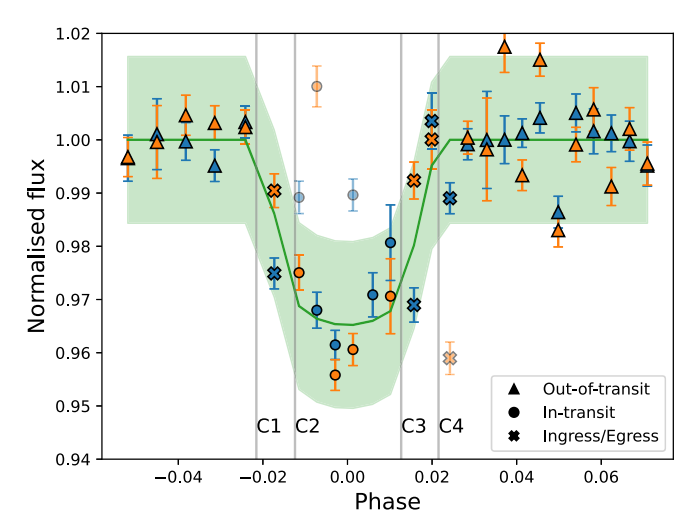


Figure 20. Frame clipping for WASP-52b. The transit light curves are shown for order 70 (blue) and order 71 (orange), calculated in a 0.43 Å wide bin centered on the redder two lines of the helium triplet. These light curves are given in terms of the *excess* transit absorption. The green line shows a fit to the combined data. The shaded green region indicates ± 3 median absolute deviations from the model. Any frame falling outside this region was removed (and is shown at a lower opacity). The plot symbols show how we defined the various stages of the transit, with the first-to-fourth contact points labeled. We note that frame 11 for order 71 fell off the bottom of this figure. This figure also demonstrates the repeatibility of our signal in the two separate orders.

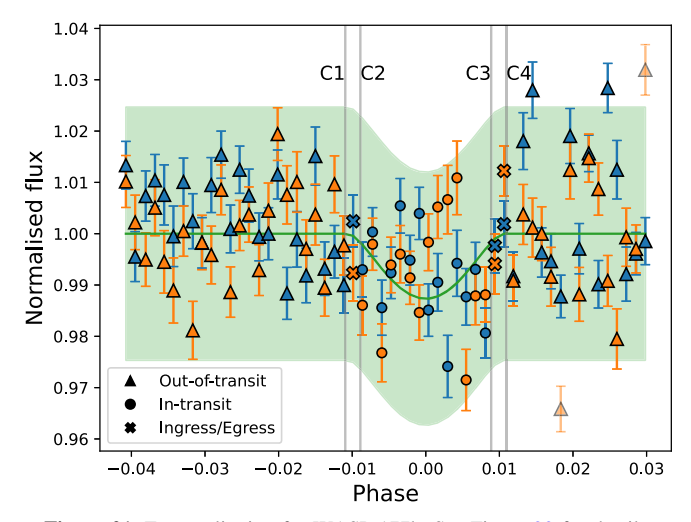


Figure 21. Frame clipping for WASP-177b. See Figure 20 for details.

ORCID iDs

James Kirk https://orcid.org/0000-0002-4207-6615 Leonardo A. Dos Santos https://orcid.org/0000-0002-2248-3838

Mercedes López-Morales https://orcid.org/0000-0003-3204-8183

Munazza K. Alam https://orcid.org/0000-0003-4157-832X Antonija Oklopčić https://orcid.org/0000-0002-9584-6476 Morgan MacLeod https://orcid.org/0000-0002-1417-8024 Li Zeng https://orcid.org/0000-0003-1957-6635 George Zhou https://orcid.org/0000-0002-4891-3517

References

Alam, M. K., Nikolov, N., López-Morales, M., et al. 2018, AJ, 156, 298 Allan, A., & Vidotto, A. A. 2019, MNRAS, 490, 3760 Allart, R., Lovis, C., Pino, L., et al. 2017, A&A, 606, A144

```
Allart, R., Bourrier, V., Lovis, C., et al. 2018, Sci, 362, 1384
Allart, R., Bourrier, V., Lovis, C., et al. 2019, A&A, 623, A58
Alonso-Floriano, F. J., Snellen, I. A. G., Czesla, S., et al. 2019, A&A,
  629, A110
Astropy Collaboration, Robitaille, T. P., Tollerud, E. J., et al. 2013, A&A,
   558, A33
Astropy Collaboration, Price-Whelan, A. M., Sipőcz, B. M., et al. 2018, AJ,
   156, 123
Baines, E. K., & Armstrong, J. T. 2012, ApJ, 744, 138
Barnes, S. A. 2007, ApJ, 669, 1167
Batalha, N. E., Mandell, A., Pontoppidan, K., et al. 2017, PASP, 129, 064501
Blanco-Cuaresma, S. 2019, MNRAS, 486, 2075
Blanco-Cuaresma, S., Soubiran, C., Heiter, U., & Jofré, P. 2014, A&A,
   569, A111
Bourrier, V., Ehrenreich, D., & Lecavelier des Etangs, A. 2015, A&A,
   582, A65
Bourrier, V., & Lecavelier des Etangs, A. 2013, A&A, 557, A124
Bourrier, V., Lecavelier des Etangs, A., Ehrenreich, D., et al. 2018, A&A,
  620, A147
Bruno, G., Lewis, N. K., Stevenson, K. B., et al. 2018, AJ, 156, 124
Bruno, G., Lewis, N. K., Alam, M. K., et al. 2020, MNRAS, 491, 5361
Carleo, I., Youngblood, A., Redfield, S., et al. 2021, AJ, 161, 136
Casasayas-Barris, N., Orell-Miquel, J., Stangret, M., et al. 2021, A&A,
  654, A163
Cauley, P. W., Kuckein, C., Redfield, S., et al. 2018, AJ, 156, 189
Chen, G., Casasayas-Barris, N., Pallé, E., et al. 2020, A&A, 635, A171
Chen, G., Pallé, E., Nortmann, L., et al. 2017, A&A, 600, L11
Czesla, S., Lampón, M., Sanz-Forcada, J., et al. 2022, A&A, 657, A6
dos Santos, L., & Vissapragada, S. 2021, ladsantos/p-winds: p-winds v1.2
   *beta*, v1.2, Zenodo, doi: 10.5281/zenodo.5513793
dos Santos, L. A., Ehrenreich, D., Bourrier, V., et al. 2020, A&A, 640, A29
Dos Santos, L. A., Vidotto, A. A., Vissapragada, S., et al. 2022, A&A,
   659, A62
Eggleton, P. P. 1983, ApJ, 268, 368
Ehrenreich, D., Bourrier, V., Wheatley, P. J., et al. 2015, Natur, 522, 459
Foreman-Mackey, D., Hogg, D. W., Lang, D., & Goodman, J. 2013, PASP,
  125, 306
Fossati, L., Guilluy, G., Shaikhislamov, I. F., et al. 2022, A&A, 658, A136
France, K., Loyd, R. O. P., Youngblood, A., et al. 2016, ApJ, 820, 89
Fulton, B. J., Petigura, E. A., Howard, A. W., et al. 2017, AJ, 154, 109
Gaia Collaboration, Prusti, T., de Bruijne, J. H. J., et al. 2016, A&A, 595, A1
Gaia Collaboration, Brown, A. G. A., Vallenari, A., et al. 2018, A&A, 616, A1
Greene, T. P., Line, M. R., Montero, C., et al. 2016, ApJ, 817, 17
Guilluy, G., Andretta, V., Borsa, F., et al. 2020, A&A, 639, A49
Hallatt, T., & Lee, E. J. 2022, ApJ, 924, 9
Hébrard, G., Collier Cameron, A., Brown, D. J. A., et al. 2013, A&A,
   549, A134
Hunter, J. D. 2007, CSE, 9, 90
Husser, T. O., Wende-von Berg, S., Dreizler, S., et al. 2013, A&A, 553, A6
Kasper, D., Bean, J. L., Oklopčić, A., et al. 2020, AJ, 160, 258
Kausch, W., Noll, S., Smette, A., et al. 2015, A&A, 576, A78
Kirk, J., Alam, M. K., López-Morales, M., & Zeng, L. 2020, AJ, 159, 115
Kirk, J., Wheatley, P. J., Louden, T., et al. 2016, MNRAS, 463, 2922
Kreidberg, L. 2015, PASP, 127, 1161
Krishnamurthy, V., Hirano, T., Stefánsson, G., et al. 2021, AJ, 162, 82
Kurokawa, H., & Nakamoto, T. 2014, ApJ, 783, 54
Lampón, M., López-Puertas, M., Lara, L. M., et al. 2020, A&A, 636, A13
Lampón, M., López-Puertas, M., Sanz-Forcada, J., et al. 2021, A&A,
```

647, A129

```
Lecavelier Des Etangs, A., Ehrenreich, D., Vidal-Madjar, A., et al. 2010, A&A,
  514, A72
Lopez, E. D., & Fortney, J. J. 2013, ApJ, 776, 2
Louden, T., Wheatley, P. J., Irwin, P. G. J., Kirk, J., & Skillen, I. 2017,
   MNRAS, 470, 742
MacLeod, M., & Oklopčić, A. 2022, ApJ, 926, 226
Mamajek, E. E., & Hillenbrand, L. A. 2008, ApJ, 687, 1264
Mancini, L., Southworth, J., Raia, G., et al. 2017, MNRAS, 465, 843
Mansfield, M., Bean, J. L., Oklopčić, A., et al. 2018, ApJL, 868, L34
Matsakos, T., & Königl, A. 2016, ApJL, 820, L8
May, E. M., Zhao, M., Haidar, M., Rauscher, E., & Monnier, J. D. 2018, AJ,
  156, 122
Mazeh, T., Holczer, T., & Faigler, S. 2016, A&A, 589, A75
McCann, J., Murray-Clay, R. A., Kratter, K., & Krumholz, M. R. 2019, ApJ,
McLean, I. S., McGovern, M. R., Burgasser, A. J., et al. 2003, ApJ, 596, 561
McLean, I. S., Prato, L., McGovern, M. R., et al. 2007, ApJ, 658, 1217
Ninan, J. P., Stefansson, G., Mahadevan, S., et al. 2020, ApJ, 894, 97
Nortmann, L., Pallé, E., Salz, M., et al. 2018, Sci, 362, 1388
Oklopčić, A. 2019, ApJ, 881, 133
Oklopčić, A., & Hirata, C. M. 2018, ApJL, 855, L11
Orell-Miquel, J., Murgas, F., Pallé, E., et al. 2022, A&A, 659, A55
Owen, J. E., & Lai, D. 2018, MNRAS, 479, 5012
Owen, J. E., & Wu, Y. 2013, ApJ, 775, 105
Owen, J. E., & Wu, Y. 2017, ApJ, 847, 29
Palle, E., Nortmann, L., Casasayas-Barris, N., et al. 2020, A&A, 638, A61
Paragas, K., Vissapragada, S., Knutson, H. A., et al. 2021, ApJL, 909, L10
Parker, E. N. 1958, ApJ, 128, 664
Parviainen, H., & Aigrain, S. 2015, MNRAS, 453, 3821
Petit dit de la Roche, D. J. M., van den Ancker, M. E., & Miles-Paez, P. A.
  2020, RNAAS, 4, 231
Poppenhaeger, K. 2022, MNRAS, 512, 1751
Redfield, S., Endl, M., Cochran, W. D., & Koesterke, L. 2008, ApJL, 673, L87
Salz, M., Czesla, S., Schneider, P. C., et al. 2018, A&A, 620, A97
Sanz-Forcada, J., Micela, G., Ribas, I., et al. 2011, A&A, 532, A6
Smette, A., Sana, H., Noll, S., et al. 2015, A&A, 576, A77
Sousa, S. G., Santos, N. C., Mayor, M., et al. 2008, A&A, 487, 373
Spake, J. J., Oklopčić, A., & Hillenbrand, L. A. 2021, AJ, 162, 284
Spake, J. J., Sing, D. K., Evans, T. M., et al. 2018, Natur, 557, 68
Tuomi, M., Anglada-Escudé, G., Gerlach, E., et al. 2013, A&A,
Turner, O. D., Anderson, D. R., Barkaoui, K., et al. 2019, MNRAS, 485, 5790
Van Der Walt, S., Colbert, S. C., & Varoquaux, G. 2011, CSE, 13, 22
Vidal-Madjar, A., Lecavelier des Etangs, A., Désert, J. M., et al. 2003, Natur,
  422, 143
Virtanen, P., Gommers, R., Oliphant, T. E., et al. 2020, NatMe, 17, 261
Vissapragada, S., Knutson, H. A., Jovanovic, N., et al. 2020, AJ, 159, 278
Wang, L., & Dai, F. 2021, ApJ, 914, 99
Wheatley, P. J., Louden, T., Bourrier, V., Ehrenreich, D., & Gillon, M. 2017,
          S, 465, L74
Wright, J. T., & Eastman, J. D. 2014, PASP, 126, 838
Wyttenbach, A., Ehrenreich, D., Lovis, C., Udry, S., & Pepe, F. 2015, A&A,
Wyttenbach, A., Lovis, C., Ehrenreich, D., et al. 2017, A&A, 602, A36
Zhang, M., Knutson, H. A., Wang, L., Dai, F., & Barragán, O. 2022a, AJ,
Zhang, M., Knutson, H. A., Wang, L., et al. 2021, AJ, 161, 181
Zhang, M., Knutson, H. A., Wang, L., et al. 2022b, AJ, 163, 68
Zhang, Y., Snellen, I. A. G., Mollière, P., et al. 2020, A&A, 641, A161
```